Efficient Tracking of Dispersion Surfaces for Printed Structures Using the Method of Moments

Denis Tihon, *Member, IEEE*, Shambhu Nath Jha, *Senior Member, IEEE*, Modeste Bodehou, *Member, IEEE*, and Christophe Craeye, *Senior Member, IEEE*

***Abstract*— The dispersion surfaces of printed periodic structures in layered media are efficiently computed using a full-wave method based on the periodic method of moments (MoM). The geometry of the dispersion surface is estimated after mapping the determinant of the periodic MoM impedance matrix over a range of frequencies and impressed phase shifts. For lossless periodic structures in the long-wavelength regime, such as lossless metasurfaces, a tracking algorithm is proposed to represent the dispersion surface as a superposition of parameterized iso-frequency curves. The mapping process of the determinant is accelerated using a specialized interpolation technique with respect to the frequency and impressed phase shifts. The algorithm combines a fast evaluation of the rapidly varying part of the periodic impedance matrix and the interpolation of the computationally intensive but slowly varying remainder. The mapping is further accelerated through the use of macro basis functions (MBFs). The method has been first tested on lossless metasurface-type structures and validated using the commercial software CST. The specialized technique enables a drastic reduction in the number of periodic impedance matrices that need to be explicitly computed. In the two examples considered, only 12 matrices are required to cover any phase shift and a frequency band larger than one octave. An important advantage of the proposed method is that it does not entail any approximation so that it can be used for lossy structure and leaky waves, as demonstrated through two additional examples.**

***Index Terms*— Dispersion curves, fast-tracking algorithm, interpolation, iso-frequency contours, macro basis functions (MBFs), metasurface, periodic structures.**

I. Introduction

ELECTROMAGNETIC fields in 2-D periodic structures have been studied for many different applications: phased arrays, photonic crystals, frequency-selective surfaces, reflect-and-transmitarrays, metamaterials, and metasurfaces. In this context, over the past four decades, the full-wave numerical analysis of such problems has been an intense subject of research [1]. The study of infinitely periodic structures is generally simplified by studying a single unit cell of the structure and imposing the periodicity of fields and currents within a linear phase shift (hereafter referred to as *quasiperiodicity*). From such analysis, global properties of the structure can be computed, such as the active impedances and reflection coefficients (both dependent on the incidence or scan angle) or homogenized equivalent sheet impedances [2], [3]. A common way to characterize fields in periodic structures corresponds to dispersion surfaces, that is, the 2-D locus of points for which a homogeneous solution to Maxwell's equations exists in the 3-D space of frequencies and impressed phase shifts, denoted, respectively, as f, ϕ_x, and ϕ_y. Many important physical quantities can be extracted from such surfaces, such as the presence of bandgaps, the Poynting vector direction, the phase and group velocities, and the dispersion of electromagnetic pulses in the material [4], with important applications in the design of new planar devices [5], [6]. Note that, in the presence of material or radiation losses, the frequencies or wave vectors can take complex values [7], [8].

The methods used to compute the dispersion curves strongly depend on the geometry studied and the hypotheses made. If the fields entering into and escaping from the unit cell can be modeled using a finite number of degrees of freedom (DoFs), the problem is mathematically simpler. First, the response of the unit cell to any external excitation is computed using a full-wave solver. Then, combining the response of the unit cell to the quasiperiodic boundary conditions, the phase shifts for which a homogeneous solution to Maxwell's equations exists can be obtained by solving a linear eigenvalue problem. This formulation naturally applies to periodic structures whose unit cells have a finite extent, as is the case for 3-D [9], [10], [11], [12], 2-D [13], [14], [15], [16], or 1-D periodic structures in 3-D, 2-D, or 1-D space, respectively, or for 1-D and 2-D periodic structures enclosed in a waveguide [6], [17], [18]. The method can also be applied to open geometries (i.e., infinite-extent unit cells) by artificially reducing the size of the unit cells using perfectly matched layers (PMLs) [19], [20] or truncating the infinite set of modes [9], [18]. However, as highlighted in [18], the selection of modes is a critical operation that may produce significant errors if not done properly. Moreover, the use of PMLs can degrade the results

Manuscript received 25 January 2023; revised 9 August 2023; accepted 22 September 2023. Date of publication 18 October 2023; date of current version 9 February 2024. *(Corresponding author: Denis Tihon.)*

Denis Tihon and Modeste Bodehou are with the ICTEAM Institute, Université catholique de Louvain (UCLouvain), 1348 Ottignies-Louvain-la-Neuve, Belgium, and also with the Fonds de la Recherche Scientifique (FNRS), 1000 Brussels, Belgium (e-mail: denis.tihon@uclouvain.be).

Shambhu Nath Jha is with Thales Belgium, 1480 Tubize, Belgium, and also with the ICTEAM Institute, Université catholique de Louvain (UCLouvain), 1348 Ottignies-Louvain-la-Neuve, Belgium.

Christophe Craeye is with the ICTEAM Institute, Université catholique de Louvain (UCLouvain), 1348 Ottignies-Louvain-la-Neuve, Belgium.

This article has supplementary material provided by the authors and color versions of one or more figures available at https://doi.org/10.1109/TAP.2023.3324083.

Digital Object Identifier 10.1109/TAP.2023.3324083

through the appearance of spurious reflections [19] or spurious guided modes [20]. Last, as illustrated in Section V-B, these methods do not handle rigorously the continuous spectrum associated with radiation into unbounded regions (or "space waves") [21], [22], [23], potentially leading to implicit approximation [18].

When dealing with truly open geometries, the computation of the dispersion curves is a nonlinear problem. First, a function of the frequency and phase shifts is chosen, whose value vanishes (resp. diverges) in the presence of a homogeneous solution to Maxwell's equations (see [24]). Then, the dispersion curves are obtained by searching for the zeros (resp. poles) of the function in the (f, ϕ_x, ϕ_y) space. This search can be carried out using iterative techniques or more involved methods based on the theory of complex analysis [25], [26]. In both cases, the function needs to be evaluated for many different phase shifts and frequencies. Using full-wave methods means that a new simulation is required at each iteration if no acceleration technique is used, leading to prohibitive computation times [27], [28]. To circumvent this problem, semianalytical models have been proposed as a tradeoff between the versatility of full-wave modeling and the rapidity of analytical models. Maci et al. [29], Patel and Grbic [30], Mencagli [31], and Pavone [32] proposed a semianalytical model for the case of subwavelength printed patches on a sufficiently thick grounded substrate. The slowly varying response of the patches is modeled using an equivalent sheet impedance. The sheet impedance is estimated using full-wave simulations and then interpolated for different phase shifts and frequencies. The impact of the substrate is added afterward using a transmission line formalism. Using this method in combination with a few additional hypotheses, an analytical description of the dispersion curves can be obtained [33].

In this article, we propose an accelerated technique for the full-wave computation of the dispersion surfaces of open 2-D periodic metallization on a stratified medium using the method of moments (MoM). The dispersion curves correspond to zeros of the determinant of the MoM impedance matrix. The acceleration relies on a specialized interpolation technique enabling a rapid sweep over frequency and phase shifts. "Specialized" here means that a limited number of potentially singular terms is first removed, such that the interpolation needs to take place only over strictly smooth functions. The potentially singular terms are reintroduced at the end on the fine grid.

To the authors' best knowledge, it is the first time that a specialized interpolation method has been proposed to handle both the impressed phase shifts and frequency. Several methods have been proposed to interpolate the periodic impedance matrix versus frequency. In [34], Hermite polynomials are used. To further accelerate the interpolation, the size of the matrix is decreased using an order reduction technique. In [35], the authors propose to add a term to the polynomial expansion that is inversely proportional to frequency. In [36], [37], [38], additional terms are added to account for the low-order Floquet modes, whose contribution can vary rapidly with frequency due to guided modes in the substrate. Last, Wang and Hum [39] propose to compute analytically the contribution of the low-order Floquet modes to reduce the number of reference matrices needed to compute the coefficients of the expansion. The method proposed in this article is an extension of the author's conference communications [40], [41], with an extension to interpolation versus frequency, reduced-order modeling of currents on the patches (see below), semiautomatic tracking of the iso-frequency contours and inclusion of radiation and substrate losses.

After the rapid interpolation of the periodic impedance matrix, its determinant is evaluated. The metallizations are modeled using the standard Rao–Wilton–Glisson [42] basis functions (BFs). Compared with specialized BFs [43], RWG have the advantage of being simple, standard, and versatile, at the expense of a less compact current representation. Given the possibly large number of unknowns required to accurately model the patches, the time required to compute the determinant of the MoM matrix over a large number of points can be prohibitive. To reduce it, the currents on the patches are limited to a smaller subspace through the use of macro BFs (MBFs) [44], leading to smaller impedance matrices. Another interpolation model is applied to the MBFs to directly interpolate the reduced impedance matrix. Using the second model, the logarithm of the determinant of the impedance matrix is rapidly evaluated on a regular grid of phase shifts and frequencies.

In addition to the fast mapping strategy, we propose a tracking procedure to extract the dispersion curves from the determinant maps for lossless structures in the long-wavelength regime. For relatively low frequencies, that is, periods smaller than a quarter wavelength (the metasurface range being rather from 10^{-1} to 2.10^{-1} wavelength), one can assume that the iso-frequency contours will be closed. Under that assumption, the contours are described by an angle-dependent radius, formulated as a Fourier series. The tracking procedure establishes a harmonic model by giving weights to each pixel of the MoM matrix determinant map versus phase shifts. An iterative refinement of the model, particularly useful in the presence of multiple iso-frequency contours, is also presented. The tracking method is semiautomatic since it involves a few parameters (e.g., relevance thresholds of pixels) that can depend on the type of patch analyzed.

It should be noted that in addition to its relatively low computation time, the proposed method offers several key advantages. First, it solely relies on the standard periodic MoM, so that it can be easily combined with existing in-house MoM software packages. Given the popularity of the MoM for the analysis of metasurfaces [45], [46], [47], [48], [49], having the possibility to study both the patches and the metasurface using the same code will greatly simplify the procedure. Second, the proposed technique does not entail any simplifying hypothesis. It rigorously models the propagation of the field along the periodic structure, handling both surface and space waves [21], [22], [23]. Third, thanks to the fast interpolation technique described, the computational cost of the proposed technique compares well with commercial software.

The remainder of this article is organized as follows. In Section II, a fast MoM procedure to compute the periodic impedance matrices is presented (Section II-A).

Then, the interpolation procedure and MBF-based compression are described (Section II-B). In Section III, we present the fast-tracking algorithm. In Section IV, the proposed method is successfully applied to metasurface-type lossless periodic structures. The treatment of lossy structures or leaky modes requiring additional care, examples featuring conduction or radiation losses are presented in Section V. It demonstrates the potential of the proposed technique to deal with damped modes and radiation.

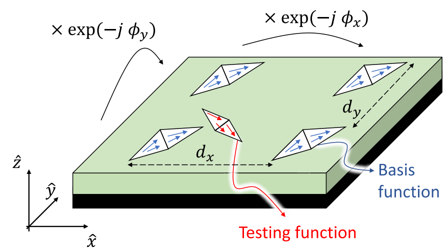

Fig. 1. Geometry considered for the interpolation procedure.

II. Fast MoM Solution

To map the determinant of the impedance matrix on a regular grid, the periodic MoM has been accelerated using several techniques. First, the computation of the periodic impedance matrix at a few reference locations has been accelerated through the tabulation of the periodic Green's function (PGF) in layered media. Then, using the reference impedance matrices, a specialized interpolation model is devised. Last, the size of the matrix is reduced using MBFs. These different steps are described in this section.

A. Computation of the Periodic Impedance Matrix

The periodic MoM impedance matrix is computed through the convolution of a tabulated PGF with the basis and testing functions (TFs). The accuracy is improved by using a singularity extraction technique similar, but not identical, to [50].

The PGF of layered media is generally computed in the spectral domain, where its value is known analytically [51]. However, the convergence of the spectral series may be slow. Moreover, its tabulation in the spatial domain is challenging due to Green's function spatial singularity. To accelerate the convergence of the spectral series, the PGF is divided into two parts: the PGF in a homogeneous equivalent medium and a corrective term [52]. The permittivity of the equivalent homogeneous medium corresponds to the average between that of the dielectric medium and the upper medium (usually air), such that the spectral series of the corrective term converges rapidly. The homogeneous medium PGF is evaluated using a "line-by-line" approach, described in [53]. The fields generated by each line of infinitesimal dipoles are expressed using a cylindrical-wave expansion. For each term of the expansion, the contribution of different lines is added up in the space domain, with an acceleration based on the Levin-T formula [54]. To limit the number of required cylindrical harmonics, the contribution of the line closest to the observation point is estimated in the spatial domain, with the use of the same accelerator. The contribution of the closest dipole is excluded to ease the tabulation of the PGF.

Once the PGF has been tabulated, it is numerically convolved with the basis and TF in the space domain [55]. The contribution of the closest dipole, which was excluded from the PGF, is evaluated in the spatial domain using standard (nonperiodic) MoM, benefiting from well-established singularity extraction procedures [56]. Since only the singularity associated with the closest source has been extracted, when basis and TFs are almost one unit cell apart, the singularity stemming from a neighboring source may appear; that singularity is avoided by shifting the PGF by one period while introducing a corrective phase shift.

Using this method, the interaction between a periodic array of BFs and a given TF can be computed for any combination of phase shifts and frequency. However, the resulting matrix is not a smooth function. This is why a new scheme is described in Section II-B, in which the singular terms are isolated and computed analytically, while the remainder is interpolated versus phase shifts.

B. Interpolation of the Periodic Impedance Matrix

The interpolation procedure described here is an extension of [40], [41] by some of the authors to include interpolation versus frequency. It is based on the observation that sharp variations of the impedance matrix can be traced back to the sharp variation of a small number of Floquet modes in the infinite spectral series. Thus, the contribution of the troublesome Floquet modes is computed explicitly and the remainder is interpolated using a reduced number of reference points. The method shows some similarities, which was proposed by Wang and Hum [39]. However, there are some major differences. First, the proposed method also deals with the interpolation versus phase shifts. Second, it is based on a less restrictive set of hypotheses, reducing the number of sampling points required for the interpolation. Last, the interpolation model is directly built on a reduced set of impedance matrices with no hypothesis on how the latter were computed. In this way, one does not need to explicitly evaluate the slowly converging infinite spectral series. Efficient hybrid spatial–spectral formulations can be used to compute the MoM periodic impedance matrices, significantly improving the computation time. In this work, we used the method described in Section II-A.

Let us consider the interaction between a quasiperiodic array of BFs and a TF above a substrate, as illustrated in Fig. 1. The array is quasiperiodic in directions $\hat{\mathbf{x}}$ and $\hat{\mathbf{y}}$ parallel to the substrate, with periods d_x and d_y. For simplicity, we consider orthogonal directions. However, generalization to nonorthogonal directions is straightforward. The BFs are identical within phase shifts ϕ_x and ϕ_y between consecutive unit cells in the $\hat{\mathbf{x}}$ and $\hat{\mathbf{y}}$ directions, respectively. The direction normal to the substrate is denoted as $\hat{z}$, with positive z above the substrate. For simplicity, we consider that there is no overlap between the BFs and TF in the direction $\hat{z}$, that is, $\exists z_0$ such that $\forall z \in$ BF and $z' \in$ TF, $(z - z_0) \times (z' - z_0) \leq 0$. This condition is, for example, automatically satisfied for flat structures printed on a substrate.

Using the Floquet theorem, the impedance matrix entry corresponding to the interaction between the BFs and the TF can be expressed as a sum of Floquet modes, that is, plane waves whose transverse wavevectors $\mathbf{k}_{t,pq} = (k_{x,p}, k_{y,q}, 0)$ satisfy the quasi-periodic condition

$$k_{x,p} = \frac{\phi_x + p2\pi}{d_x} \tag{1}$$

$$k_{y,q} = \frac{\phi_y + q2\pi}{d_y}. \tag{2}$$

To simplify the calculations, for a given plane wave, we consider the $\hat{\mathbf{e}}$, $\hat{\mathbf{m}}$, and $\hat{\mathbf{k}}$ directions defined as

$$\hat{\mathbf{e}} = \frac{1}{k_t}\big(-k_y, k_x, 0\big) \tag{3}$$

$$\hat{\mathbf{m}}^{\pm} = -\frac{1}{k_0 k_t}\big(\pm k_z^{\uparrow} k_x, \pm k_z^{\uparrow} k_y, -k_t^2\big) \tag{4}$$

$$\hat{\mathbf{k}}^{\pm} = \frac{1}{k_0}\big(k_x, k_y, \pm k_z^{\uparrow}\big) \tag{5}$$

with k_0 being the free-space wavenumber, $k_t = (\mathbf{k}_t \cdot \mathbf{k}_t)^{1/2}$ the transverse wavenumber, and $k_z^{\uparrow} = (k_0^2 - k_t^2)^{1/2}$ the vertical (upward) wavenumber. The + sign corresponds to the plane waves directed upward (i.e., toward the $\hat{z}$-direction) and the − sign corresponds to plane waves directed downward. Note that, in this article, the square root function is defined such that its phase lies in $[-\pi, 0]$, such that the imaginary part of $k_z^{\uparrow}$ is ≤ 0. Using this special set of directions, the periodic impedance matrix describing the electric field generated on the TF by the electric current on the periodic BFs can be expressed as

$$\begin{aligned} Z^{J\to E} = {} & \frac{\eta_0 k_0}{d_x d_y} \sum_{p=-\infty}^{\infty} \sum_{q=-\infty}^{\infty} \frac{1}{2k_{z,pq}^{\uparrow}} \\ & \times \Big(\tilde{f}_{B,e}\big(\mathbf{k}_{pq}^{\pm}\big) \tilde{f}_{T,e}\big(-\mathbf{k}_{pq}^{\pm}\big) \\ & \quad + \tilde{f}_{B,e}\big(\mathbf{k}_{pq}^{-}\big) \tilde{f}_{T,e}\big(-\mathbf{k}_{pq}^{+}\big) \Gamma^{\mathrm{TE}}\big(\mathbf{k}_{t,pq}\big) \\ & \quad + \tilde{f}_{B,m^{\pm}}\big(\mathbf{k}_{pq}^{\pm}\big) \tilde{f}_{T,m^{\pm}}\big(-\mathbf{k}_{pq}^{\pm}\big) \\ & \quad + \tilde{f}_{B,m^{-}}\big(\mathbf{k}_{pq}^{-}\big) \tilde{f}_{T,m^{+}}\big(-\mathbf{k}_{pq}^{+}\big) \Gamma^{\mathrm{TM}}\big(\mathbf{k}_{t,pq}\big) \Big) \end{aligned} \tag{6}$$

where η_0 is the free-space impedance, $k_{z,pq}^{\uparrow}$ is the $k_z^{\uparrow}$ wavenumber associated with Floquet mode (p, q), and Γ^{TE} and Γ^{TM} correspond to the reflection coefficients of TE and TM waves on the substrate and the Fourier transform of the BF and TF are defined as

$$\tilde{f}_{B/T,i}(\mathbf{k}) = \hat{\mathbf{i}} \cdot \iint \mathbf{f}_{B/T}(\mathbf{r}) \exp\big(j\mathbf{k} \cdot \mathbf{r}\big) d\mathbf{r} \tag{7}$$

with $\mathbf{f}_B(\mathbf{r})$ and $\mathbf{f}_T(\mathbf{r})$ as the value of the BF and TF at position $\mathbf{r}$. Unit vector $\hat{\mathbf{i}}$ can be either $\hat{\mathbf{e}}$ or $\hat{\mathbf{m}}$ [(3) or (4)]. Note that the first and third terms in (6) correspond to the contribution of TE and TM waves to the free-space interaction between the BFs and TF, and the sign should be chosen to correspond to the geometry (BFs above or below the TF). For BFs and TFs on the same plane, any sign can be chosen.

Similarly, the magnetic field generated on the TF by electric currents on the BF reads

$$\begin{aligned} Z^{J\to H} = {} & \frac{k_0}{d_x d_y} \sum_{p=-\infty}^{\infty} \sum_{q=-\infty}^{\infty} \frac{1}{2k_{z,pq}^{\uparrow}} \\ & \times \Big(\tilde{f}_{B,e}\big(\mathbf{k}_{pq}^{\pm}\big) \tilde{f}_{T,m^{\pm}}\big(-\mathbf{k}_{pq}^{\pm}\big) \\ & \quad + \tilde{f}_{B,e}\big(\mathbf{k}_{pq}^{-}\big) \tilde{f}_{T,m^{+}}\big(-\mathbf{k}_{pq}^{+}\big) \Gamma^{\mathrm{TE}}\big(\mathbf{k}_{t,pq}\big) \\ & \quad - \tilde{f}_{B,m^{\pm}}\big(\mathbf{k}_{pq}^{\pm}\big) \tilde{f}_{T,e}\big(-\mathbf{k}_{pq}^{\pm}\big) \\ & \quad - \tilde{f}_{B,m^{-}}\big(\mathbf{k}_{pq}^{-}\big) \tilde{f}_{T,e}\big(-\mathbf{k}_{pq}^{+}\big) \Gamma^{\mathrm{TM}}\big(\mathbf{k}_{t,pq}\big) \Big). \end{aligned} \tag{8}$$

To efficiently interpolate the impedance matrix, a good understanding of the evolution of $Z^{J\to E}$ and $Z^{J\to H}$ with phase shifts and frequency is required. This article concentrates on the analysis of $Z^{J\to E}$. However, $Z^{J\to H}$ can be treated similarly.

A detailed analysis of $Z^{J\to E}$ (see Appendix A) shows that the contributions of a limited set of low-order Floquet modes can exhibit sharp variations and is thus difficult to interpolate. However, the contribution of high-order Floquet modes evolves smoothly with frequency and phase shifts. Moreover, for small BF and TF, evolution with frequency is roughly proportional to $1/k_0$, while evolution with phase shift corresponds to a linear phase shift proportional to the relative positions of the BF and the TF.

Exploiting these observations, an efficient interpolation method can be devised. First, as classically done (see [39], [57], [58]), the total impedance matrix is split into two parts: one corresponding to visible and slightly evanescent Floquet modes (i.e., of orders below chosen thresholds N_x, N_y: $-N_x \leq p \leq N_x, -N_y \leq q \leq N_y$), denoted as $Z_v^{J\to E}$, and one corresponding all the other Floquet modes, denoted as $Z_e^{J\to E}$

$$Z^{J\to E}(k_0, \phi_x, \phi_y) = Z_v^{J\to E}(k_0, \phi_x, \phi_y) + Z_e^{J\to E}(k_0, \phi_x, \phi_y). \tag{9}$$

The values of N_x and N_y depend on the dimensions of the unit cell and are typically of the order of $0, \ldots, 2$ for a metasurface. Provided that N_x and N_y are small enough, the computation of the first term is very rapid: the reflection coefficient is independent of the pair of BF and TF considered and is thus only computed once, and the Fourier transforms of the BF and TF can be evaluated separately and combined afterward. Note that the latter is true only because we considered BF and TF with no overlap in the $\hat{z}$-direction. If there is an overlap, the formulation of (6) should be slightly modified, so that the factors related to the BF and TF are no longer separable for the free-space interaction.

Concerning the second term of (9), evaluating it using the infinite series of Floquet modes can be time-consuming. Moreover, the absence of low-order Floquet modes can impede the use of specialized acceleration techniques, such as the one described in Section II-A. However, it can be easily interpolated after a few minor modifications, namely multiplication by a phase factor and by the frequency. Thus, the raw periodic impedance matrix $Z^{J\to E}$ is evaluated on a few phase shifts and frequencies. Then, for each sampling point, $Z_v^{J\to E}$ is evaluated and subtracted from the total impedance matrix. Last, a phase

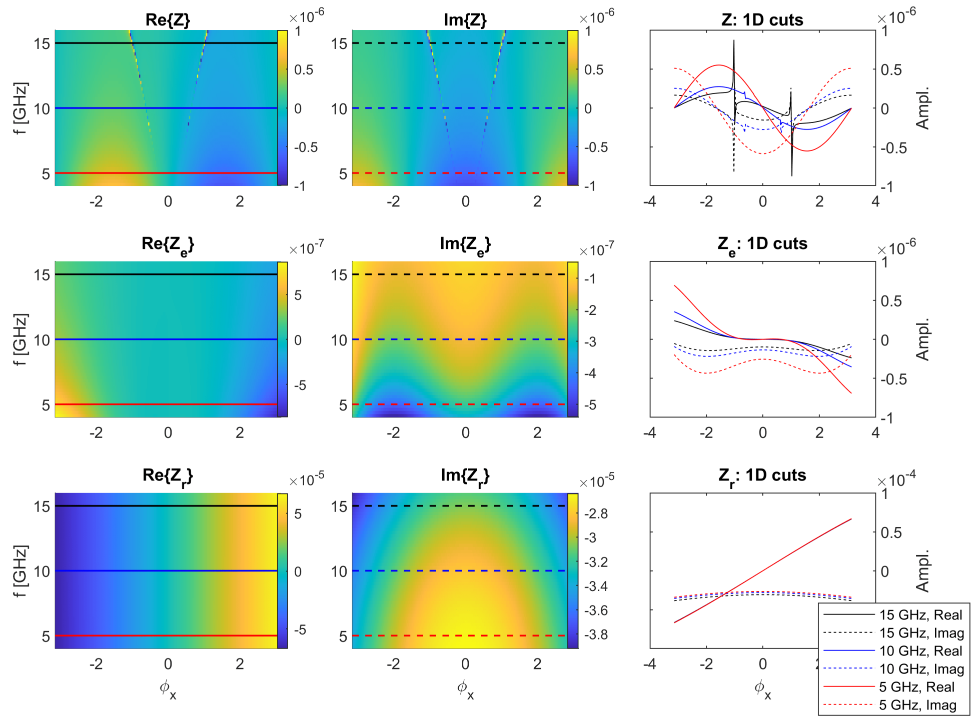

Fig. 2. Evolution of the $Z^{J\to E}$ (top), $Z_e^{J\to E}$ (middle), and $Z_r^{J\to E}$ (bottom) terms with frequency and phase shift for a typical pair of Rao–Wilton–Glisson basis and TFs. The real part of the function (left). The imaginary part of the function (middle). One-dimensional cuts at 5, 10, and 15 GHz (right). The continuous line corresponds to the real part and the dashed line to the imaginary part. The progressive smoothing of the function with each consecutive step is clearly visible.

term proportional to the average lateral distance Δx and Δy between the BF and TF is removed, the result is multiplied by k_0, and the remainder, denoted as $Z_r^{J\to E}$, is interpolated

$$Z_r^{J\to E} = k_0 \exp\left(j\left(\frac{\phi_x \Delta x}{d_x} + \frac{\phi_y \Delta y}{d_y}\right)\right) \times \left(Z^{J\to E} - Z_v^{J\to E}\right). \tag{10}$$

Interpolation is carried out using a multidimensional polynomial. Excellent results are obtained due to the very smooth function obtained after removing the contribution of the main Floquet modes, the phase factor, and the inverse frequency. As an illustration, the evolution of the $Z^{J\to E}$, $Z_e^{J\to E}$, and $Z_r^{J\to E}$ terms with frequency and phase shift is illustrated in Fig. 2 for a typical pair of BF and TF separated by half a unit cell.

Once the polynomial interpolation model for $Z_r^{J\to E}$ has been built, the interpolation procedure can be summarized as follows. First, the $Z_r^{J\to E}$ term is interpolated. Then, the $Z_v^{J\to E}$ term is computed as a small series of Floquet modes. The impedance matrix entry is then obtained using

$$Z^{J\to E} = Z_v^{J\to E} + \frac{Z_r^{J\to E}}{k_0} \exp\left(-j\left(\frac{\phi_x \Delta x}{d_x} + \frac{\phi_y \Delta y}{d_y}\right)\right). \tag{11}$$

Using this procedure, the periodic impedance matrix (and its determinant) can be rapidly evaluated over a fine grid of phase shifts and frequencies. To further accelerate the technique, three computational bottlenecks have been identified and alleviated/solved. First, to build a 3-D polynomial interpolation model, a large number of reference matrices need to be computed. Second, when interpolating the impedance matrix using (11), most of the time is devoted to the evaluation of the Fourier transform of the BF and TF, even when analytical formulas are available (e.g., in the case of RWG [42] or rooftop BF and TF). Last, for large meshes, the interpolation procedure asymptotically scales as the square of the number of unknowns, and the evaluation of the determinant as its cubic power, rapidly increasing the computation time with the mesh density.

To mitigate the first bottleneck, we exploited the 2π periodicity of the periodic impedance matrix versus ϕ_x and ϕ_y. Since $Z^{J\to E}$ is periodic, once $Z^{J\to E}(\phi_x, \phi_y)$ has been computed, $Z^{J\to E}(\phi_x + 2m\pi, \phi_y + 2n\pi)$ does not provide any additional information and thus cannot be used as such to improve the interpolation model. However, the choice of the Floquet modes that are removed depends on the phase shifts considered since $k_{x,p}(\phi_x) = k_{x,(p-1)}(\phi_x + 2\pi) \neq k_{x,p}(\phi_x + 2\pi)$ [see (1)]. Thus, $Z_r^{J\to E}$ is not periodic: its values at positions $Z^{J\to E}(\phi_x, \phi_y)$ and $Z^{J\to E}(\phi_x + 2m\pi, \phi_y + 2n\pi)$ (with m or n different from zero) convey complementary information and can thus be used to improve the interpolation model. Thus, the same periodic matrix can be used to extract the value of $Z_r^{J\to E}$ at several different phase shifts separated by a distance 2π. Even if, eventually, the interpolation model of $Z_r^{J\to E}$ only needs to cover the first Brillouin zone, it can be improved using sampling points located outside of this zone provided that $Z_r^{J\to E}$ is smooth over the extended zone. Thus, there is a tradeoff that can be optimized: the zone over which $Z_r^{J\to E}$ is smooth can be extended by increasing N_x and N_y, reducing the number of periodic impedance matrices required to build the model. However, the cost of evaluating $Z_v^{J\to E}$ increases with N_x and N_y, which impacts all the subsequent interpolations. In practice, we observed that slightly increasing N_x and N_y (from $N_x, N_y = 0$ to $N_x, N_y = 1$ in the examples considered) and using sampling points over the zone $[-2\pi, 2\pi]$ was beneficial to the accuracy and total computation time. For a given frequency, only four periodic impedance matrices $Z^{J\to E}$ were required to build a 2-D fourth-order polynomial model.

To remove the second bottleneck and accelerate the evaluation of the Fourier transform of the BFs and TFs, we used a polynomial interpolation technique. First, an average phase term related to the mean position of the BF or TF is removed. Then, the remainder is fit using a polynomial model. For BFs and TFs that are not horizontal, special care is required to handle the angular point related to the visibility limit and thus the angular behavior of $k_z^\uparrow$. However, for coplanar horizontal BF and TF, the $k_z^\uparrow$ factor has no impact on the interpolant, simplifying the interpolation procedure. In the geometries studied, excellent accuracy has been obtained with relatively low polynomial orders (around order 5), further accelerating the computations.

Last, to reduce the number of unknowns, a model order reduction (MOR) [13], [34] technique based on MBFs [44] has been used. First, using the interpolation model, we compute the equivalent current distribution generated on the periodic structure by incident plane waves with various transverse wave vectors and at various frequencies. A reduced basis that can reproduce all the current distributions within a prescribed accuracy is built. Each vector of this new basis (i.e., MBF) corresponds to a linear combination of BFs. Projecting the full impedance matrices into the new basis, one obtains a reduced impedance matrix that can serve as an accurate approximation of the original one. More information about the procedure can be found in Appendix B.

Once the set of MBFs has been obtained, the interpolation procedure described previously is applied to the reduced matrices. On the one hand, the reduced number of unknowns leads to smaller matrices, that is, less entries that need to be interpolated and a faster evaluation of the determinant. On the other hand, MBFs have a larger spatial extent than BFs, so that their Fourier transforms are less smooth. Higher-order interpolation models are thus required to interpolate the Fourier transform of the MBFs and the $Z_r^{J\to E}$ terms. In the examples studied, the use of MBFs accelerated the mapping of the determinant by a factor ranging from 3.5 to 8. This factor accounts for the time devoted to the computation of the MBFs.

C. Summary of the Algorithm

The algorithm used to interpolate the reduced impedance matrix is summarized below. The algorithm has been split into two parts. First, the preparation (P) corresponds to the computation of the MBFs and the establishment of the interpolation model. It only needs to be carried out once for a given geometry. Then, the interpolation (I) itself must be repeated for each new combination of frequency and phase shifts at which the reduced impedance matrix is required.

Preparation:

- *P1:* Build an interpolation model for the Fourier transform of the BFs and TFs.
- *P2:* Sample the interpolant of the periodic impedance matrix ($Z_r^{J\to E}$) at several phase shifts and frequencies, that is, as follows.
  - *P2.1:* Compute the periodic impedance matrix (or use a previously computed matrix).
  - *P2.2:* Remove the contributions of the low-order Floquet modes.
  - *P2.3:* Remove the phase factor and multiply by the frequency.
- *P3:* Build a polynomial model that can approximate the interpolant.
- *P4:* Build the MBFs.
- *P5:* Sample the interpolant ($Z_r^{J\to E}$) of the reduced impedance matrix for several phase shifts and frequencies, that is, as follows.
  - *P5.1:* Interpolate the $Z_r^{J\to E}$ term of the full-size impedance matrix.
  - *P5.2:* Add the phase factor.
  - *P5.3:* Project the matrix into the MBFs.
  - *P5.4:* Remove the phase factor associated with the MBFs.
- *P6:* Build a polynomial model that can approximate the new interpolant.
- *P7:* Build an interpolation model for the Fourier transform of the MBFs.

Interpolation:

- *I1:* Interpolate the $Z_r^{J\to E}$ term of the MBF-compressed impedance matrix.
- *I2:* Multiply by the phase factor and divide by the frequency.
- *I3:* Add the contributions of the low-order Floquet modes.
- *I4:* Compute the logarithm of the determinant of the reduced impedance matrix.

Note that when MBFs are defined over the entire metallization, the average distance between two different MBFs is zero, so that the phase factors mentioned in steps P5.4 and I2 simply correspond to a factor of 1.

III. Tracking Algorithm

A. Choice of the Metric

To track the dispersion curves, we chose to map the determinant of the periodic impedance matrix. Tracking the determinant has several advantages and disadvantages over other metrics, such as the conditioning number or the so-called *characteristic term* [24]. On the one hand, using the determinant, it is possible to distinguish between zeros and poles of the matrix (i.e., diverging or vanishing eigenvalues) or to use complex-analysis based techniques since the value of the determinant is an analytic function of the entries of the matrix. On the other hand, if the number of unknowns is large, the computation of the determinant can be costly and prone to overflow or underflow error using standard arithmetic precision.

For the geometries studied, the computational cost was found to be acceptable, thanks to the use of MBFs. To avoid

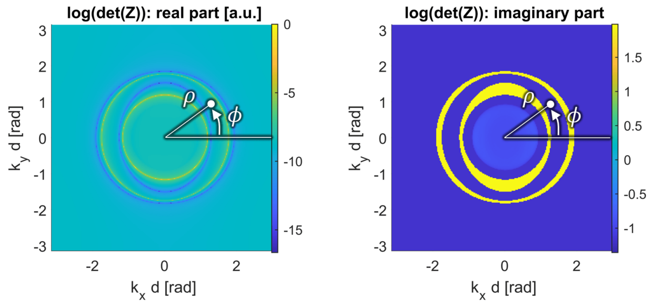

Fig. 3. Map of the real (left) and imaginary (right) parts of the logarithm of the determinant for a typical geometry. Poles and zeros of the determinant are characterized by an increase (yellow) or decrease (blue) of the real part of its logarithm, respectively, and a sharp change of its imaginary part.

overflow or underflow errors, we chose to compute the logarithm of the determinant instead of the determinant itself. The amplitude and phase of the determinant are directly related to the real and imaginary parts of its logarithm, respectively. To compute the logarithm of the determinant without explicitly computing the determinant, the following identity has been used:

$$\det\{A\} = k^N \det\{A/k\} \tag{12}$$

with A being an $N \times N$ matrix (here, N is the number of MBFs) and k a scalar. The logarithm of the determinant then becomes

$$D_r + jD_i = \log\big(\det\{A\}\big) = N\log(k) + \log\big(\det\{A/k\}\big). \tag{13}$$

The actual value of the logarithm was found iteratively. First, a factor k is used to "rescale" the matrix. The value of k can be obtained from a priori information, such as the value of the determinant for frequencies or phase shifts that are close. If the determinant of the scaled impedance matrix is `inf` (resp. `0`), the k factor is rescaled by a factor $10^{-280/N}$ (resp. $10^{280/N}$), with 10^{280} that is slightly smaller than the maximum number that can be represented using standard `double` precision and N the size of the impedance matrix. Using this method, the value of the determinant is generally obtained after a few iterations when no a priori information is available, and at the first iteration otherwise.

B. Computation of Dispersion Surfaces

For lossless surface waves (SWs), the dispersion surfaces in the (f, ϕ_x, ϕ_y) space are computed as stacks of iso-frequency contours in successive (ϕ_x, ϕ_y) planes. In each plane, the logarithm of the determinant of the reduced impedance matrix is mapped. Iso-frequency curves are associated with a vanishing determinant, that is, a real part of its logarithm going to $-\infty$. A typical map of the real and imaginary parts of its logarithm for a lossless open periodic structure is provided in Fig. 3. Different features can be observed. First, inside the visible region, the phase of the determinant can vary smoothly, due to the presence of radiation loss. Since the frequency and phase shifts are real, no sharp variation is expected, with poles and zeros being located at complex coordinates (i.e., complex frequencies and/or phase shifts). Outside the visible zone, there is no radiation loss, so that sharp variations of the amplitude and phase associated with zeros and poles of the determinant are visible. Poles are associated with SWs of the substrate (i.e., poles of the PGF), while zeros are associated with iso-frequency contours. In addition to poles and zeros, features associated with Wood's anomalies (i.e., branch points in the PGF due to grazing incidence of the main or secondary lobes) may appear.

The determination of iso-frequency contours developed here assumes a closed curve in the (ϕ_x, ϕ_y)-plane. Using polar coordinates (ρ, ϕ), each contour is parameterized using a harmonic model versus angular coordinate ϕ

$$\rho_i(\phi) = c_i + \sum_n \big(d_{i,n}\cos(n\phi) + e_{i,n}\sin(n\phi)\big) \tag{14}$$

with i corresponding to the index of the curve.

To find the coefficients of the harmonic expansion, a weight is attributed to each pixel of the map, with larger weights attributed to pixels that are expected to be close to the curve.

The weight depends on several indicators. The first one obviously depends on the log-magnitude of the determinant, corresponding to $D_r(\phi_x, \phi_y)$ (13). It is taken as $D_r(0, 0) - D_r(\phi_x, \phi_y)$. The next indicator corresponds to the local variation of the determinant versus phase shifts ϕ_x and ϕ_y. More precisely, it is computed as $|\partial D_r/\partial\psi_x| + |\partial D_r/\partial\psi_y|$. If a previous estimate of the model, $\rho_p(\phi)$, is available (see below), the proximity to the model also appears as a useful indicator, for example, $\exp(-|\rho(\phi)-\rho_p(\phi)|^2/(2\sigma^2))$, where σ is smaller when the previous estimation is deemed more reliable. The first two indicators are multiplied with each other and the result should be larger than a given threshold μ. The third indicator is used to exclude pixels that are too far from a previous estimate if available. Using these weights, the determination of coefficients c_i, $d_{i,n}$, and $e_{i,n}$ becomes a weighted least-squares problem, the goal being to minimize the rms radial distance between each pixel and the curve. Mathematically, it amounts to solving the over-constrained system of equations

$$w \cdot M\,x = w \cdot \rho \tag{15}$$

where each line corresponds to a given pixel of the map. w is a column vector containing the weights associated with each pixel, x is a column vector containing all the model coefficients $(c_i, d_{i,n}, e_{i,n})$, ρ is a column vector containing the radial coordinate of the pixels, and M is a matrix whose columns correspond to vectors 1, $\cos(n\phi)$, and $\sin(n\phi)$ for all n. The dot multiplication $(\cdot)$ here means column-wise element-by-element multiplication. Pixels with a low weight, typically below threshold $\mu = 0.16$, can be excluded from the system of equations to reduce the computation time. It can be noted that some other parameters may have to be tuned based on the type and the complexity of the patches under consideration. For instance, in the case of rectangular patches (Section IV-A), the harmonic order needed is 2, while for the case of a more complex structure, such as coffee bean patch (Section IV-B), for which several contours appear, that order needs to be increased to 6. In terms of the σ parameter, related to proximity with previous estimates, for both cases, it remains identical and is equal to 0.04π rad.

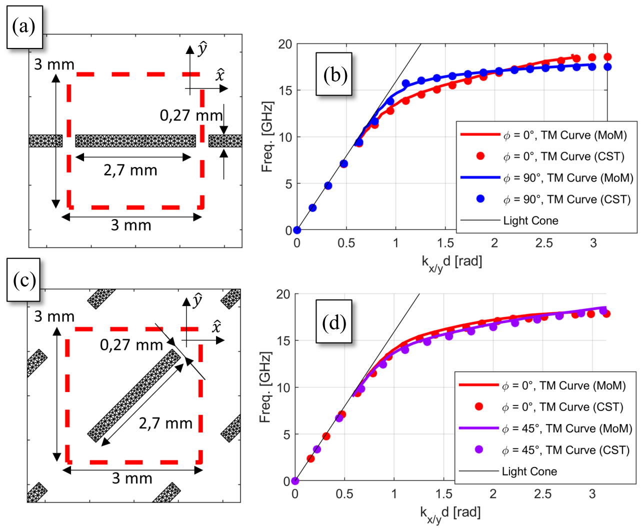

Fig. 4. (a) and (c) Geometry of the two arrays of rectangular patches studied. (b) and (d) Dispersion curves obtained using the method described in this work and the commercial software CST [61].

In case two contours are observed, the outer one is first modeled. Larger weights are provided to pixels of the outer contour (when compared to pixels of the inner contour) by providing larger weights for larger values of ρ. Then, an iterative refinement only accounting for pixels close to the previous estimate can be used to better catch the outer curve. Once the position of the outer curve has been estimated with sufficient precision, the inner curve position can be determined by excluding the contribution of the pixels that are close to or outside the estimate of the outer curve. Iterating, the cross-influence between different curves can be rapidly eliminated.

IV. Numerical Results: Lossless Case

The interpolation method and the tracking algorithm have been tested on different arrays of printed patches: square arrays of rectangular patches with varying orientations and a square array of coffee-bean patches proposed in [59] and [60] for the design of leaky-wave metasurface antennas.

The same numerical parameters have been used for two geometries to interpolate the periodic impedance matrix. To build the interpolation model of the impedance matrix itself, only three sampling points have been used versus frequency. For each frequency, only four periodic matrices associated with phase shifts $\phi_x, \phi_y \in \{0, \pi\}$ have been computed using the method described in Section II-A. From these 12 matrices, $Z_r^{J\to E}$ has been estimated at 75 locations, for phase shifts ranging from -2π to 2π, by extracting the nine dominant Floquet modes ($N_x = N_y = 1$). Using these points, the slowly varying term $Z_r^{J\to E}$ (see (10)) was interpolated using a 3-D polynomial of orders 4, 4, and 2 along the ϕ_x, ϕ_y, and f dimensions, respectively. The polynomial interpolation of the Fourier transform of the BF and TF over the whole zone of interest was carried out using a 2-D polynomial of orders 5 along both the k_x and k_y dimensions.

Once the interpolation model was built, the MBFs were computed considering 3645 different plane-wave excitations of various frequencies and wavevectors. The thresholds $\theta_1 = 10^{-3}$ and $\theta_2 = 10^{-15}$ have been chosen (see Appendix B), leading to 20 and 11 MBFs (depending on the orientation) in the case of the rectangular patches and 86 MBFs in the case of coffee-bean patches. The interpolation of the reduced impedance matrix was done using polynomials of order 9, 9, and 4 along the ϕ_x, ϕ_y, and f dimensions, respectively. Their Fourier transform was interpolated using polynomials of orders 11 along k_x and k_y. Note that, using this set of parameters, the relative error introduced by the whole interpolation procedure on the entries of the reduced impedance matrix was estimated to be below 10^{-3}.

TABLE I

Time Required to Obtain the Dispersion Curves of the $\hat{x}$-Directed Rectangular Patches and the Coffee-Bean Patches

Mesh	Rectangles (325 BF)	coffee beans (348 BF)
Preparation time [s]		
Computation of periodic impedance matrices (12)	138	155
Preparation of the interpolation models	3	3.1
Computation of the MBFs	12.5	13.3
Preparation of the interpolation models for MBFs	10	21
Total	164	192
Mapping of the determinant and tracking of the curves [s]		
Mapping	263	508
Tracking	0.25	16

Last, the determinant has been mapped over a regular grid of 100 × 100 × 30 points versus ϕ_x, ϕ_y, and f, respectively. The computation of the full dispersion surfaces in the real $\phi_x - \phi_y - f$ space took approximately 10 min for the rectangular patches (see Figs. 4 and 5) and 15 min for the coffee-bean patches (see Fig. 6). For comparison, using the same computer, the computation of the reference results obtained using CST [61] [see dots in Figs. 4(b) and (d) and 6(c))] took approximately 15 and 5 min, respectively. It is important to note that CST results only correspond to 1-D cuts of the full dispersion surfaces and that the CST computations were fully parallelized.

The detailed timing of the whole procedure is provided in Table I. The simulations were run on a `i7-10700` processor without any parallelization, except for the computation of the determinant using the `det` built-in MATLAB function. It can be noticed that the time is dominated by the mapping of the determinant over a large number of points. This time could be reduced by adaptively choosing where the MoM impedance matrices need to be evaluated, as the zeros of the determinant are being tracked in the $f - \phi_x - \phi_y$ domain. Such refined techniques are out of the scope of the article.

A. Rectangular Patch

The dispersion surfaces of periodic arrays of rectangular patches have been studied at frequencies ranging from 9 to 20 GHz. The patches are deposited on a 1-mm-thick grounded dielectric substrate of relative permittivity 9.8.

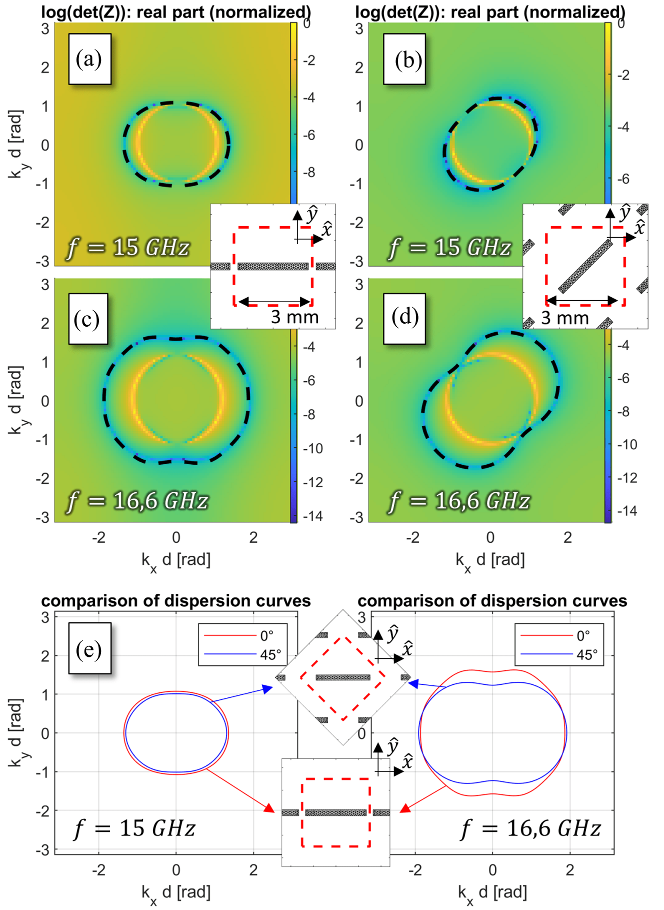

Fig. 5. Iso-frequency curves of the arrays of rectangular patches (a) and (c) aligned with the $\hat{\mathbf{x}}$-direction and (b) and (d) rotated by 45°, 15, and 16.6 GHz. The estimated dispersion curves (dashed black line) are superimposed on the map of the absolute value of the determinant, in a logarithmic scale. (e) Comparison of the iso-frequency curves of both arrays. Note that the iso-frequency curve of the 45°-rotated patches has been rotated again to facilitate the comparison.

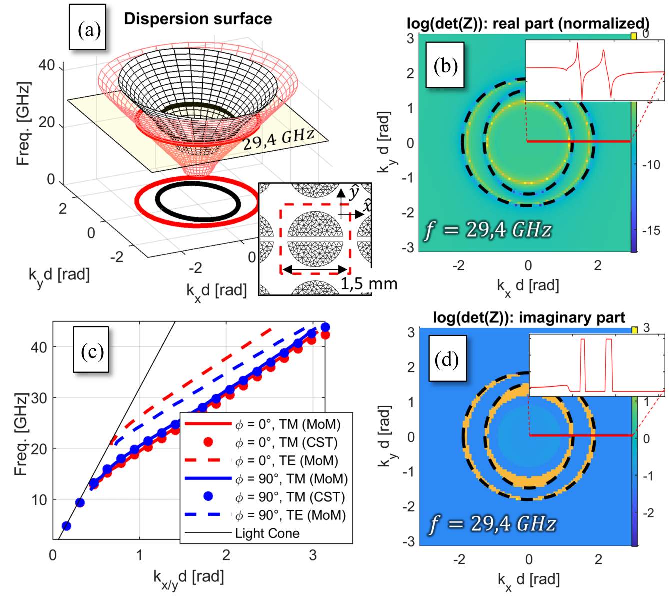

Fig. 6. (a) Dispersion surface of the coffee-bean patches (see inset). (c) Dispersion curves of the (quasi-)TM and TE modes obtained using the proposed method and using CST. (b) and (d) Iso-frequency curves (black dashed lines) of the TE (inner curve) and TM (outer curve) modes at 29.4 GHz. They are superimposed on the map of the (b) real part and (d) imaginary part of the logarithm of the determinant. Finely sampled transverse cuts along the direction $\phi = 0$ are illustrated in the insets.

The patches have been discretized using 325 RWG BFs. In one configuration, the patches are aligned with the direction of periodicity. In the other configuration, they are rotated by 45°. Both geometries are illustrated in Fig. 4(a) and (c).

It is well known that, at low frequencies, this structure supports the propagation of a dominant TM SW. The dispersion curves of both patches have been computed for a fixed azimuthal direction ϕ (see conventions in Fig. 3) and validated using the eigenmode solver of the CST commercial software [61]. To use the eigenmode solver, the simulation zone has been truncated using a perfectly conducting plane located sufficiently far away from the periodic structure to prevent evanescent coupling between the structure and the plane. Since the surface mode does not radiate into free space, accurate results could be obtained in this way. As shown in Fig. 4(b) and (d), the dispersion curves obtained by both means match very well.

To look at the impact of the rotation of the patches, the iso-frequency curves of both arrays have been displayed in Fig. 5 at frequencies of 15 and 16.6 GHz, along with the map of the logarithm of the amplitude of the determinant. As expected, the iso-frequency dispersion curve is less circular at higher frequencies, which means that the response of the structure is more anisotropic. To highlight the impact of the rotation of the patches, the iso-frequency curves of the two arrays are compared in Fig. 5(e). It is observed that at lower frequencies, the effect of the rotation of the patch can be accurately estimated by simply rotating the dispersion curve. However, moving to higher frequencies, this is no longer true because of the different relative positions of the patches.

It should be noted that, although our interpolation technique is valid at any frequency, the proposed eigenmode tracking method assumes a closed iso-frequency dispersion curve due to the harmonic expansion along azimuth used in (14). This assumption is only valid as long as the unit cells are sufficiently subwavelength, limiting the maximum frequency. However, this condition is usually met for metasurfaces, in which the homogenization assumption imposes subwavelength unit cells. A different eigenmode tracking algorithm is required at higher frequencies, for example, when studying bandgap materials.

B. Coffee-Bean Patches

A periodic array of coffee-bean patches has been studied at frequencies between 10 and 45 GHz. The patches correspond to circles of radius 600 μm that are split into two parts by a 120-μm slit. The patches have been discretized using 348 BFs and are illustrated in the inset of Fig. 6(a). The patches are deposited on a 1.5-mm-thick grounded substrate of relative permittivity 6, with a periodicity of 1.5 mm. This patch type has been proposed in [59] and [60] for the design of leaky-wave metasurface antennas.

The dispersion surfaces of the patches are displayed in Fig. 6(a). It can be noticed that, at high frequency, two different surfaces are visible, corresponding to the quasi-TM (red) and quasi-TE (black) modes. The iso-frequency curves at 29.4 GHz have been extracted from the surfaces and are displayed in Fig. 6(b) and (d) (black dashed line). They are superimposed on the map of the real and imaginary parts of the logarithm of the determinant. As explained in Section III-B, the dispersion curves correspond to zeros of the determinant and are thus associated with a phase jump of π [Fig. 6(d)].

Cuts of the dispersion surface in the planes $\phi = 0$ and $\phi = 90°$ are provided in Fig. 6(c), as well as a comparison with CST results for the quasi-TM mode. A very good agreement is obtained.

V. Numerical Results: Lossy Case

The surface modes can be damped due to the presence of radiation or conduction losses. The study of lossy surface modes is more delicate. The coordinates of the lossy modes in the $f - \phi_x - \phi_y$ space are complex, and the imaginary part is related to the damping coefficient. Thus, in addition to an increased algorithmic complexity (the search space is $\mathbb{C}^3$ instead of $\mathbb{R}^3$), more fundamental problems arise, such as the definition of the branch cuts associated with each branch point of the PGF or the definition of "physical" modes (i.e., modes that can be physically excited). To address these questions, we use the approach proposed in [21], [22], and [23]: the goal is to compute the propagation of the fields along the $\hat{\mathbf{x}}$-direction so that branch cuts follow the steepest descent path from the branch points and only poles located on the top Riemann sheet below the real ϕ_x-axis are considered. Using this formalism, the fields propagating along the surface can be split into two contributions: the contribution of the branch cuts (space waves) and the contributions of the poles (surface mode). While the position of the former is known in the complex plane, the position (or even existence) of the latter is not, from there the need to find them to characterize the periodic structure.

Given the presence of complex phase shifts, the automated tracking procedure described in Section III-B cannot be used. However, the specialized interpolation procedure and the mapping of the determinant can be straightforwardly extended to deal with complex phase shifts or frequencies. In this section, we study two different geometries taken from [9] supporting lossy modes.

A. Meandered Microstrip Line on a Lossy Substrate

The first geometry corresponds to a meandered microstrip enclosed in a parallel-plate waveguide. The geometry of the microstrip is displayed in Fig. 7(a). It is deposited on a 0.3-mm-thick grounded dielectric layer of relative permittivity $\varepsilon_r = 3.6(1 + 0.0015j)$. The air layer between the microstrip and the upper conducting plane is 0.3 mm thick. The structure supports a slightly damped strongly anisotropic guided wave [9].

The determinant of the impedance matrix versus real phase shifts at 30 GHz is displayed in Fig. 7(b) and (d). Two closed

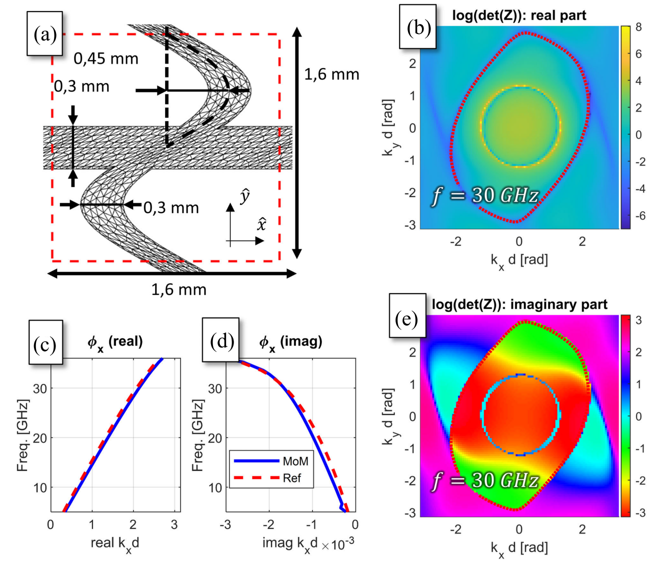

Fig. 7. (a) Geometry of the microstrip enclosed in the lossy parallel-plate waveguide. (b) and (e) Map of the real and imaginary parts of the determinant of the periodic impedance matrix at 30 GHz. The red dashed line corresponds to the reference results from [9]. (c) and (d) Real and imaginary parts of the propagation constant of one of the guided modes in the $\hat{\mathbf{x}}$-direction ($k_y d = 0$, $f = 30$ GHz). The results of [9] extracted using the Engauge Digitizer software [62] have been added for comparison (red dashed line).

curves with a small value of the determinant are separated by a closed curve with a high value. The high-value curve coincides with the pole of the PGF (i.e., due to the fundamental mode of the parallel-plate waveguide in the absence of the printed microstripline). The two low-value curves correspond to the two guided modes supported by the waveguide in the presence of the microstrip. Since the geometry includes three different 2-D-connected conducting structures, the presence of two different quasi-TEM modes was expected. It can be seen that the shape of the outer curve matches nearly perfectly the results of [9] (red dashed line).

In addition to the two guided modes, two regions with a low value of the determinant can be seen on the left- and right-hand sides of Fig. 7(b) and (e). These are numerical artifacts associated with the MoM itself. They are very sensitive to the mesh or the number of MBFs used and can thus be easily discriminated from real guided modes.

Due to the presence of losses, the determinant never perfectly vanishes for real phase shifts. To find the zeros of the determinant, one needs to look at the complex $\phi_x - \phi_y$ space. Given the increased dimensionality of the problem, we imposed $\phi_y = 0$ and mapped the determinant in the complex ϕ_x-plane. The automated tracking of the zero in the complex plane is out of the scope of this article, and we extracted manually its position as a function of frequency. The results are visible in Fig. 7(c) and (d). It can be seen that the proposed method (blue line) compares very well with the prediction of [9] (red dashed line).

B. Leaky Waveguide

To study the impact of radiation losses, another structure of [9] has been studied. It consists of a periodic square array

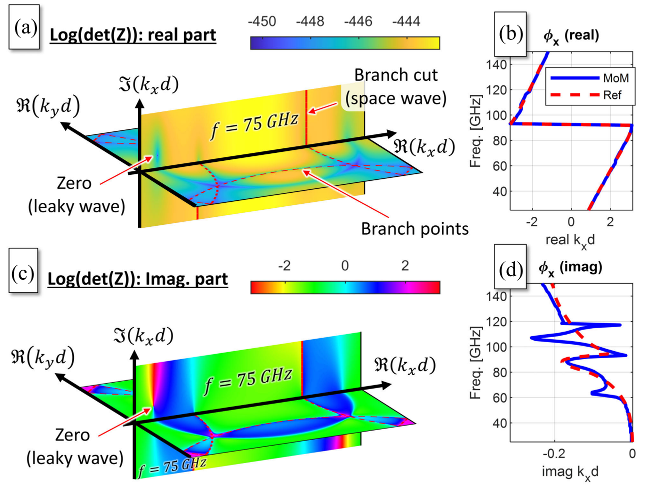

Fig. 8. (a) and (c) Evolution of the real and imaginary parts of the logarithm of the determinant over the first Brillouin zone for real and complex phase shifts. The position of the branch points (dashed red curves) and branch cuts (continuous red curves) are highlighted. (b) and (d) Real and imaginary parts of the complex coordinate of the leaky wave for $\mathbb{I}\{\phi_x\} < 0$ and $\phi_y = 0$. The results of [9], collected using [62], are superimposed for comparison.

of holes in a conducting sheet. The holes correspond to 0.8-mm-side squares that are repeated every 1.6 mm in the $\hat{\mathbf{x}}$- and $\hat{\mathbf{y}}$-directions. The sheet is separated from the ground plane by a 0.5-mm air layer. The half-space above the sheet is made of a dielectric material with a relative permittivity of 3.6. Since the permittivity of the upper half-space is higher than the permittivity of the air layer, the "surface" modes correspond to fast waves that radiate. Given the radiation losses, the phase shifts associated with these modes are complex.

As explained in the previous section, mapping the determinant over the 5-D space corresponding to complex phase shifts and real frequency is not tractable. For this reason, we looked at the determinant of the impedance matrix for complex ϕ_x when $\phi_y = 0$ [vertical plane in Fig. 8(a) and (c)]. The zeros have been manually extracted from the determinant map at each frequency. The position of the leaky mode versus frequency is shown in Fig. 8(b) and (d) and compared with the results from [9].

The two curves nearly perfectly coincide for the real part of ϕ_x. However, the imaginary parts largely differ. First, a peak of the attenuation constant is visible around 63 GHz. This peak is associated with the appearance of a grating lobe at that combination of frequency and the real part of the phase shift (Wood's anomaly). To properly handle this grating lobe, one needs to account for the associated space wave (continuous spectrum corresponding to the branch cut contribution). While the periodic impedance matrix of the MoM rigorously accounts for it, the simplified transfer matrix of [9] does not. It may thus miss the possibly long-range interplay between the space wave and the leaky mode [23]. Similarly, the oscillations between 93 and 118 GHz are associated with the proximity of another branch cut. At 118 GHz, the oscillating leaky mode crosses a branch cut and is replaced by a more stable leaky mode coming from the other Riemann sheet. To better illustrate the complex interactions between the zeros and the branch cuts, a video showing the evolution of the position of the zeros and branch cuts with frequency is available in the Supplementary Material.

VI. Conclusion

A fast eigenmode tracking technique for periodic printed structures based on the MoM has been proposed. The method is based on an efficient interpolation of the MoM impedance matrix, followed by a mapping of its determinant for various phase shifts and frequencies, and a tracking of the eigenmodes. One major advantage of the proposed interpolation method is the extremely small number of periodic impedance matrices that need to be computed explicitly. In the examples presented, only 2×2 matrices are needed to interpolate their value over the first Brillouin zone at a given frequency, and only three sampling frequencies are required to interpolate their value over more than an octave. An excellent agreement has been obtained with the results from the CST commercial software. The main advantage of the proposed method with respect to the quasianalytical methods described in the literature is the fact that it is directly built on the MoM. Therefore, it can handle arbitrary metallizations including connected ones, and very thin substrates, where semianalytical methods may be inaccurate due to the interaction of higher-order Floquet modes with the ground plane. The applicability of the proposed method to lossy structures and leaky waves has been demonstrated through several examples.

Appendix A
Detailed Analysis of $Z^{J\to E}$

To efficiently interpolate the impedance matrix for varying phase shifts and frequencies, we have here a deeper look at the way $Z^{J\to E}$ varies with phase shift and frequency. Looking at (6), different factors involved in each Floquet term can be highlighted [41]. For simplicity, the Fourier transform of the BF and TF are separated into two factors: the Fourier transform of the $x - y - z$ components of the BF and TF [integral in (7)] and the $\hat{\mathbf{e}}$ and $\hat{\mathbf{m}}$ unit vectors.

1) *k_0 prefactor:* It is proportional to the frequency.
2) *$1/k_{z,pq}^{\uparrow}$ factor:* For high-order Floquet modes ($k_{t,pq} \gg k_0$), the derivative of this factor with frequency and phase shifts asymptotically scales as $1/k_{t,pq}^3$ and $1/k_{t,pq}^2$, respectively, that is, variation gets smaller as the Floquet mode order increases.
3) *Γ^{TE} and Γ^{TM} factors:* The interpolation of those factors may be complicated due to the presence of angular points, branch points, and poles. The two former are due to the visibility limits in the different materials involved in the substrate. The latter is due to SWs supported by the substrate. As a rule of thumb, the reflection coefficients exhibit smooth variation when $k_{t,pq} \gg k_{\max}$, with $k_{\max}$ being the wavenumber in the material with the largest refractive index.
4) *Fourier transform of the BF and TF:* Changes in the value of the Fourier transform are induced by a change of the $\mathbf{k}_{pq}^{\pm}$ vector, which can itself be decomposed into changes in $\mathbf{k}_{t,pq}$ and $k_{z,pq}^{\uparrow}$. For small BF and TF,

variation with $\mathbf{k}_{t,pq}$ is quite predictable and corresponds approximately to a linear phase shift that depends on the lateral distance between the BF and TF. This phase shift is identical for all the Floquet modes and can thus be extracted easily. For large BF or TF, deviation from a linear phase shift increases. However, it should be noted that the size of the BF and TF is ultimately limited by the size of the unit cell, which also dictates the maximum variation versus $\mathbf{k}_{t,pq}$. Hence, in the worst-case scenario, interpolation can still provide satisfactory results, be it at the cost of a higher interpolation model. Concerning the variation of $k^{\uparrow}_{z,pq}$, we concentrate on the evolution of high-order Floquet modes. Such modes are highly evanescent so that two cases can be highlighted. If the vertical distance between the BF and TF is short, a small change in $k^{\uparrow}_{z}$ leads to a small relative variation of the Fourier transform. If the distance is large, then the product of the two Fourier transforms vanishes.

5) $\hat{\mathbf{e}}$ *and* $\hat{\mathbf{m}}$ *directions:* Rapid changes in the directions are possible when $k_{t,pq} \rightarrow 0$ or near the visibility limit. However, for high-order Floquet modes, the variation with phase shift is quite smooth. It can be noticed that $\hat{\mathbf{e}}$ is independent of frequency, while $\hat{\mathbf{m}}$ is inversely proportional to the frequency.

Appendix B
Size Reduction Using MBFs

MOR techniques are based on the observation that the response of a structure to electromagnetic fields can be modeled accurately using a limited number of DoFs [13], [44], hereafter referred to as *physical DoFs*. Using the MoM, those physical DoFs generally correspond to current distributions spanning over the entire structure. However, most electromagnetic solvers use BFs locally defined on a mesh to model the response of the structure. These *numerical* DoFs generally poorly match the physical ones. Hence, to get accurate results, a dense mesh with many extra numerical DoFs is required. The basic idea of MOR techniques is to find, among all the numerical DoFs, those that are close to physical DoFs and discard the others. The MBF method consists of computing the response of the structure to a large set of different excitations [44]. Then, an orthonormal basis is built to approximate these responses within a chosen accuracy. In the case of the MoM, each vector of the basis corresponds to a current distribution that is close to a physical DoF of the structure.

To build the MBFs of the structure, we used a technique similar to [44]. The fast interpolation technique is used to get the periodic impedance matrix for several phase shifts and frequencies (see Section II-B). Then, the response of the structure to plane waves corresponding to low-order Floquet modes is computed. The resulting current distributions are concatenated in a large matrix, and a singular value decomposition (SVD) is applied to the matrix. A threshold θ_1 is chosen. Modes whose singular value is smaller than the maximum singular value by a factor exceeding θ_1 are discarded.

To limit the number of current distributions that should be kept in memory, intermediate SVDs are used. For any new phase shift and frequency, the newly computed current distributions are appended to the already computed singular vectors. Then, an SVD is applied to the matrix, creating a new orthonormal basis that includes the new excitations. Then, a threshold θ_2 is chosen, and singular vectors whose singular value (relative to the maximum singular value) is smaller than the threshold are discarded. We used a threshold θ_2 that is less restrictive than θ_1 to limit the impact of the intermediate SVDs on the final results obtained.

For the testing procedure, we used a set of macro TFs (MTFs) equal to that of the MBFs. We did not observe a significant difference in the results using MTFs equal to the MBFs or equal to their complex conjugate.

The use of MBFs allows us to deal with significantly smaller matrices when searching for roots of the determinant.

Acknowledgment

Denis Tihon and Modeste Bodehou are Postdoctoral Researchers of the Fond de la Recherche Scientifique (FNRS).

References

[1] C. Craeye, X. Radu, A. Schuchinsky, and F. Capolino, "Fundamentals of method of moments for metamaterials," in *Handbook of Metamaterials*, F. Capolino, Ed. New York, NY, USA: Taylor Francis, Jun. 2009.

[2] M. A. Francavilla, E. Martini, S. Maci, and G. Vecchi, "On the numerical simulation of metasurfaces with impedance boundary condition integral equations," *IEEE Trans. Antennas Propag.*, vol. 63, no. 5, pp. 2153–2161, May 2015.

[3] G. Minatti et al., "Metasurface antennas," in *Aperture Antennas for Millimeter and Sub-Millimeter Wave Applications*, A. Boriskin and R. Sauleau, Eds. Cham, Switzerland: Springer, 2018, ch. 9, pp. 289–333.

[4] S. Enoch, G. Tayeb, and B. Gralak, "The richness of the dispersion relation of electromagnetic bandgap materials," *IEEE Trans. Antennas Propag.*, vol. 51, no. 10, pp. 2659–2666, Oct. 2003.

[5] M. Mencagli, E. Martini, D. González-Ovejero, and S. Maci, "Metasurfing by transformation electromagnetics," *IEEE Antennas Wireless Propag. Lett.*, vol. 13, pp. 1767–1770, 2014.

[6] Q. Chen, F. Giusti, G. Valerio, F. Mesa, and O. Quevedo-Teruel, "Anisotropic glide-symmetric substrate-integrated-holey metasurface for a compressed ultrawideband Luneburg lens," *Appl. Phys. Lett.*, vol. 118, no. 8, Feb. 2021, Art. no. 084102.

[7] M. Dehmollaian and C. Caloz, "General mapping between complex spatial and temporal frequencies by analytical continuation," *IEEE Trans. Antennas Propag.*, vol. 69, no. 10, pp. 6531–6545, Oct. 2021.

[8] J. G. N. Rahmeier, V. Tiukuvaara, and S. Gupta, "Complex eigenmodes and eigenfrequencies in electromagnetics," *IEEE Trans. Antennas Propag.*, vol. 69, no. 8, pp. 4644–4656, Aug. 2021.

[9] F. Giusti, Q. Chen, F. Mesa, M. Albani, and O. Quevedo-Teruel, "Efficient Bloch analysis of general periodic structures with a linearized multimodal transfer-matrix approach," *IEEE Trans. Antennas Propag.*, vol. 70, no. 7, pp. 5555–5562, Jul. 2022.

[10] A. A. Tavallaee and J. P. Webb, "Finite-element modeling of evanescent modes in the stopband of periodic structures," *IEEE Trans. Magn.*, vol. 44, no. 6, pp. 1358–1361, Jun. 2008.

[11] Y. Xiong, J. A. Russer, W. Che, G. Shen, Y. Han, and P. Russer, "Dispersion analysis of a fishnet metamaterial based on the rotated transmission-line matrix method," *IET Microw., Antennas Propag.*, vol. 9, no. 12, pp. 1345–1353, Sep. 2015.

[12] D. Tihon, V. Sozio, N. A. Ozdemir, M. Albani, and C. Craeye, "Numerically stable eigenmode extraction in 3-D periodic metamaterials," *IEEE Trans. Antennas Propag.*, vol. 64, no. 7, pp. 3068–3079, Jul. 2016.

[13] C. Scheiber, A. Schultschik, O. Bíró, and R. Dyczij-Edlinger, "A model order reduction method for efficient band structure calculations of photonic crystals," *IEEE Trans. Magn.*, vol. 47, no. 5, pp. 1534–1537, May 2011.

[14] P.-J. Chiang, C.-P. Yu, and H.-C. Chang, "Analysis of two-dimensional photonic crystals using a multidomain pseudospectral method," *Phys. Rev. E, Stat. Phys. Plasmas Fluids Relat. Interdiscip. Top.*, vol. 75, no. 2, Feb. 2007, Art. no. 026703.

[15] H. Y. D. Yang, "Finite difference analysis of 2-D photonic crystals," *IEEE Trans. Microw. Theory Techn.*, vol. 44, no. 12, pp. 2688–2695, Mar. 1996.

[16] L. Tsang and S. Tan, "Calculation of band diagrams and low frequency dispersion relation of 2D periodic dielectric scatterers using broadband green's function with low wavenumber extraction (BBGFL)," *Opt. Exp.*, vol. 24, no. 2, pp. 945–965, 2016.

[17] M. Bagheriasl, O. Quevedo-Teruel, and G. Valerio, "Bloch analysis of artificial lines and surfaces exhibiting glide symmetry," *IEEE Trans. Microw. Theory Techn.*, vol. 67, no. 7, pp. 2618–2628, Jul. 2019.

[18] F. Mesa, G. Valerio, R. Rodríguez-Berral, and O. Quevedo-Teruel, "Simulation-assisted efficient computation of the dispersion diagram of periodic structures: A comprehensive overview with applications to filters, leaky-wave antennas and metasurfaces," *IEEE Antennas Propag. Mag.*, vol. 63, no. 5, pp. 33–45, Oct. 2021.

[19] P. Bienstman, H. Derudder, R. Baets, F. Olyslager, and D. De Zutter, "Analysis of cylindrical waveguide discontinuities using vectorial eigenmodes and perfectly matched layers," *IEEE Trans. Microw. Theory Techn.*, vol. 49, no. 2, pp. 349–354, Feb. 2001.

[20] S. Shi, C. Chen, and D. W. Prather, "Plane-wave expansion method for calculating band structures of photonic crystal slabs with perfectly matched layers," *J. Opt. Soc. Amer. A, Opt. Image Sci.*, vol. 21, no. 9, pp. 1769–1775, 2004.

[21] T. Tamir and A. A. Oliner, "Guided complex waves. Part 1: Fields at an interface," *Proc. Inst. Electr. Eng.*, vol. 110, no. 2, pp. 310–324, 1963.

[22] F. Capolino, D. R. Jackson, and D. R. Wilton, "Fundamental properties of the field at the interface between air and a periodic artificial material excited by a line source," *IEEE Trans. Antennas Propag.*, vol. 53, no. 1, pp. 91–99, Jan. 2005.

[23] F. Capolino, D. R. Jackson, and D. R. Wilton, "Field representation in periodic artificial materials excited by a source," in *Theory and Phenomena of Metamaterials*, F. Capolino, Ed. Boca Raton, FL, USA: CRC Press, 2009, pp. 12.1–12.26.

[24] X. Zheng et al., "Implementation of the natural mode analysis for nanotopologies using a volumetric method of moments (V-MoM) algorithm," *IEEE Photon. J.*, vol. 6, no. 4, pp. 1–13, Aug. 2014.

[25] L. M. Delves and J. N. Lyness, "A numerical method for locating the zeros of an analytic function," *Math. Comput.*, vol. 21, no. 100, pp. 543–560, 1967.

[26] D. A. Bykov and L. L. Doskolovich, "Numerical methods for calculating poles of the scattering matrix with applications in grating theory," *J. Lightw. Technol.*, vol. 31, no. 5, pp. 793–801, Dec. 20, 2013.

[27] H. Alaeian and R. Faraji-Dana, "A fast and accurate analysis of 2-D periodic devices using complex images green's functions," *J. Lightw. Technol.*, vol. 27, no. 13, pp. 2216–2223, Jul. 15, 2009.

[28] H. Ameri and R. Faraji-Dana, "Green's function analysis of electromagnetic wave propagation in photonic crystal devices using complex images technique," *J. Lightw. Technol.*, vol. 29, no. 3, pp. 298–304, Dec. 23, 2011.

[29] S. Maci, M. Caiazzo, A. Cucini, and M. Casaletti, "A pole-zero matching method for EBG surfaces composed of a dipole FSS printed on a grounded dielectric slab," *IEEE Trans. Antennas Propag.*, vol. 53, no. 1, pp. 70–81, Jan. 2005.

[30] A. M. Patel and A. Grbic, "Modeling and analysis of printed-circuit tensor impedance surfaces," *IEEE Trans. Antennas Propag.*, vol. 61, no. 1, pp. 211–220, Jan. 2013.

[31] M. Mencagli, E. Martini, and S. Maci, "Surface wave dispersion for anisotropic metasurfaces contstituted by elliptical patches," *IEEE Trans. Antennas Propag.*, vol. 63, no. 7, pp. 2992–3003, Jul. 2015.

[32] S. C. Pavone, E. Martini, F. Caminita, M. Albani, and S. Maci, "Surface wave dispersion for a tunable grounded liquid crystal substrate without and with metasurface on top," *IEEE Trans. Antennas Propag.*, vol. 65, no. 7, pp. 3540–3548, Jul. 2017.

[33] M. Mencagli, C. D. Giovampaola, and S. Maci, "A closed-form representation of isofrequency dispersion curve and group velocity for surface waves supported by anisotropic and spatially dispersive metasurfaces," *IEEE Trans. Antennas Propag.*, vol. 64, no. 6, pp. 2319–2327, Jun. 2016.

[34] D. S. Weile, E. Michielssen, and K. Gallivan, "Reduced-order modeling of multiscreen frequency-selective surfaces using Krylov-based rational interpolation," *IEEE Trans. Antennas Propag.*, vol. 49, no. 5, pp. 801–813, May 2001.

[35] A. S. Barlevy and Y. Rahmat-Samii, "Characterization of electromagnetic band-gaps composed of multiple periodic tripods with interconnecting vias: Concept, analysis, and design," *IEEE Trans. Antennas Propag.*, vol. 49, no. 3, pp. 343–353, Mar. 2001.

[36] L. Li, D. H. Werner, J. A. Bossard, and T. S. Mayer, "A model-based parameter estimation technique for wide-band interpolation of periodic moment method impedance matrices with application to genetic algorithm optimization of frequency selective surfaces," *IEEE Trans. Antennas Propag.*, vol. 54, no. 3, pp. 908–924, Mar. 2006.

[37] X. Wang and D. H. Werner, "Improved model-based parameter estimation approach for accelerated periodic method of moments solutions with application to the analysis of convoluted frequency selected surfaces and metamaterials," *IEEE Trans. Antennas Propag.*, vol. 58, no. 1, pp. 122–131, Jan. 2010.

[38] X. Wang, D. H. Werner, and J. P. Turpin, "Application of AIM and MBPE techniques to accelerate modeling of 3-D doubly periodic structures with nonorthogonal lattices composed of bianisotropic media," *IEEE Trans. Antennas Propag.*, vol. 62, no. 8, pp. 4067–4080, Aug. 2014.

[39] Z. Wang and S. V. Hum, "A broadband model-based parameter estimation method for analyzing multilayer periodic structures," *IEEE Trans. Antennas Propag.*, vol. 69, no. 9, pp. 5771–5780, Sep. 2021.

[40] D. Tihon, M. Bodehou, S. N. Jha, and C. Craeye, "Fast eigenmode mapping in printed periodic structures," in *Proc. 16th Eur. Conf. Antennas Propag. (EuCAP)*, Mar. 2022, pp. 1–5.

[41] D. Tihon, C. Craeye, N. Ozdemir, and S. Withington, "Interpolation of impedance matrices for varying quasi-periodic boundary conditions in 2D periodic method of moments," in *Proc. 15th Eur. Conf. Antennas Propag. (EuCAP)*, Mar. 2021, pp. 1–5.

[42] S. Rao, D. Wilton, and A. Glisson, "Electromagnetic scattering by surfaces of arbitrary shape," *IEEE Trans. Antennas Propag.*, vol. AP-30, no. 3, pp. 409–418, May 1982.

[43] M. Camacho, R. R. Boix, and F. Medina, "NUFFT for the efficient spectral domain MoM analysis of a wide variety of multilayered periodic structures," *IEEE Trans. Antennas Propag.*, vol. 67, no. 10, pp. 6551–6563, Oct. 2019.

[44] E. Lucente, A. Monorchio, and R. Mittra, "An iteration-free MoM approach based on excitation independent characteristic basis functions for solving large multiscale electromagnetic scattering problems," *IEEE Trans. Antennas Propag.*, vol. 56, no. 4, pp. 999–1007, Apr. 2008.

[45] S. Sandeep and S. Y. Huang, "Simulation of circular cylindrical metasurfaces using GSTC-MoM," *IEEE J. Multiscale Multiphys. Comput. Techn.*, vol. 3, pp. 185–192, 2018.

[46] J. Budhu and A. Grbic, "Perfectly reflecting metasurface reflectarrays: Mutual coupling modeling between unique elements through homogenization," *IEEE Trans. Antennas Propag.*, vol. 69, no. 1, pp. 122–134, Jan. 2021.

[47] S. Pearson and S. V. Hum, "Optimization of electromagnetic metasurface parameters satisfying far-field criteria," *IEEE Trans. Antennas Propag.*, vol. 70, no. 5, pp. 3477–3488, May 2022.

[48] D. González-Ovejero and S. Maci, "Gaussian ring basis functions for the analysis of modulated metasurface antennas," *IEEE Trans. Antennas Propag.*, vol. 63, no. 9, pp. 3982–3993, Sep. 2015.

[49] J. Cavillot, M. Bodehou, and C. Craeye, "Metasurface antennas design: Full-wave feeder modeling and far-field optimization," *IEEE Trans. Antennas Propag.*, vol. 71, no. 1, pp. 39–49, Jan. 2023.

[50] R. Florencio, R. R. Boix, and J. A. Encinar, "Fast and accurate MoM analysis of periodic arrays of multilayered stacked rectangular patches with application to the design of reflectarray antennas," *IEEE Trans. Antennas Propag.*, vol. 63, no. 6, pp. 2558–2571, Jun. 2015.

[51] D. Pozar and D. Schaubert, "Scan blindness in infinite phased arrays of printed dipoles," *IEEE Trans. Antennas Propag.*, vol. AP-32, no. 6, pp. 602–610, Jun. 1984.

[52] S. N. Jha, "Fast spectral-domain macro basis function analysis of large arrays of printed antennas," Ph.D. dissertation, ICTEAM Inst., Université catholique de Louvain, Louvain-la-Neuve, Belgium, Aug. 2014.

[53] N. Guerin, C. Craeye, and X. Dardenne, "Accelerated computation of the free space green's function gradient of infinite phased arrays of dipoles," *IEEE Trans. Antennas Propag.*, vol. 57, no. 10, pp. 3430–3434, Oct. 2009.

[54] S. Singh and R. Singh, "On the use of Levin's T-transform in accelerating the summation of series representing the free-space periodic green's functions," *IEEE Trans. Microw. Theory Techn.*, vol. 41, no. 5, pp. 884–886, May 1993.

[55] C. Craeye, A. G. Tijhuis, and D. H. Schaubert, "An efficient MoM formulation for finite-by-infinite arrays of two-dimensional antennas arranged in a three-dimensional structure," *IEEE Trans. Antennas Propag.*, vol. 52, no. 1, pp. 271–282, Jan. 2004.

[56] D. Wilton, S. Rao, A. Glisson, D. Schaubert, O. Al-Bundak, and C. Butler, "Potential integrals for uniform and linear source distributions on polygonal and polyhedral domains," *IEEE Trans. Antennas Propag.*, vol. AP-32, no. 3, pp. 276–281, Mar. 1984.

[57] S. Monni, G. Gerini, A. Neto, and A. G. Tijhuis, "Multimode equivalent networks for the design and analysis of frequency selective surfaces," *IEEE Trans. Antennas Propag.*, vol. 55, no. 10, pp. 2824–2835, Oct. 2007.

[58] R. Rodríguez-Berral, F. Mesa, and F. Medina, "Analytical multimodal network approach for 2-D arrays of planar patches/apertures embedded in a layered medium," *IEEE Trans. Antennas Propag.*, vol. 63, no. 5, pp. 1969–1984, May 2015.

[59] G. Minatti et al., "Modulated metasurface antennas for space: Synthesis, analysis and realizations," *IEEE Trans. Antennas Propag.*, vol. 63, no. 4, pp. 1288–1300, Apr. 2015.

[60] M. Bodehou, K. A. Khalifeh, S. N. Jha, and C. Craeye, "Direct numerical inversion methods for the design of surface wave-based metasurface antennas: Fundamentals, realizations, and perspectives," *IEEE Antennas Propag. Mag.*, vol. 64, no. 4, pp. 24–36, Aug. 2022.

[61] Dassault Systemes. *CST Studio Suite, Electromagnetics Simulation Software*. Accessed: Aug. 2023. [Online]. Available: https://www.3ds.com/products-services/simulia/products/cst-studio-suite/solvers/

[62] M. Mitchell, B. Muftakhidinov, and T. Winchen. *Engauge Digitizer Software*. Accessed: Aug. 2023. [Online]. Available: http://markummitchell.github.io/engauge-digitizer

Denis Tihon (Member, IEEE) received the M.Eng. degree in physical engineering and the Ph.D. degree in electrical engineering from the Université Catholique de Louvain (UCLouvain), Ottignies-Louvain-la-Neuve, Belgium, in 2013 and 2018, respectively.

From 2013 to 2019, he was a Teaching Assistant with UCLouvain and worked on the modeling of periodic absorbers illuminated by partially coherent fields. From 2017 to 2019, he participated in the M-Cube FET-OPEN European Project during which he worked on the simulation of magnetic resonance imaging (MRI) antennas. From 2019 to 2021, he worked on the modeling and measurement of partially coherent fields from luminescent sources with the Cavendish Laboratory, University of Cambridge, Cambridge, U.K., under a Marie Sklodowska-Curie Fellowship. Since 2021, he has been a Post-Doctoral Researcher of the Fond de la Recherche Scientifique (FNRS) Belgium, continuing his research on luminescent emitters at UCLouvain. His current research interests include computational electromagnetism, the modeling of partially coherent fields, periodic and nonperiodic absorbers, luminescent light sources, and reciprocity.

Shambhu Nath Jha (Senior Member, IEEE) was born in Nepal, in 1978. He received the bachelor's degree (Hons.) in electrical engineering from the Institute of Engineering, Tribhuvan University, Kirtipur, Nepal, in 2001, the European Master of Research degree in information and communication technologies from the Universitat Politécnica de Catalunya, Barcelona, Spain, in 2008, the master's degree (cum laude) in electrical engineering, the Ph.D. degree in applied sciences (electrical engineering) from the Université Catholique de Louvain (UCL), Ottignies-Louvain-la-Neuve, Belgium, in 2009 and 2014, respectively, and the M.Sc. degree (Hons.) in management from Vrije Universiteit Brussel, Ixelles, Belgium, in 2016.

He was a Research and Development Electrical Engineer with Icoms Detections SA, Ottignies-Louvain-la-Neuve, from 2014 to 2016, where he was involved in the area of antenna and microwave circuits for a radar system for traffic control in scientific collaboration with UCL, where he was also a Research Assistant for fast analysis of antenna arrays and several government-funded projects on antenna system development, from 2009 to 2014. He is currently an electromagnetic specialist with Thales Belgium, Tubize, Belgium. He is currently collaborating with UCLouvain as a scientific collaborator to contribute to the fundamental research in the area of electromagnetics. This research contribution belongs to the framework of the intellectual property rights of UCLouvain. His current research interests include optimized antenna and radio system development for various practical applications, meta-surfaces, periodic structures, small antenna concepts, innovative shielding concepts, strategic value creation in customer requirements in a changing innovative environment, and value co-creation.

Dr. Jha was a recipient of the European Commission's Erasmus Mundus Scholarship from 2007 to 2009 and 13 other national and international academic/research grants and fellowships.

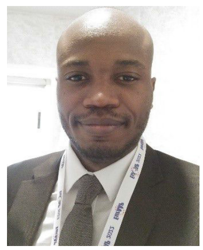

Modeste Bodehou (Member, IEEE) was born in Cotonou, Benin, in 1992. He received the B.Sc. degree in engineering and the M.Sc. degree in electrical engineering (telecommunications) from the Royal Military Academy, Brussels, Belgium, in 2013 and 2015, respectively, the Ph.D. degree in engineering and technology and the master's degree in management from the Université Catholique de Louvain, Ottignies-Louvain-la-Neuve, Belgium, in 2020 and 2022, respectively.

In 2015, he was with the Quartier Major Housiau (Belgium Defense), Vilvoorde, Belgium, where he was involved in the framework of his application school on military communication systems. He is currently an FNRS Post-Doctoral Researcher with the Microwave and Applied Electromagnetism Laboratory, Université Catholique de Louvain. His current research interests include computational electromagnetics, antenna arrays, and metasurfaces.

Dr. Bodehou was a recipient of the 2021 EurAAP Per-Simon Kildal Award for Best Ph.D. in Antennas and Propagation, the Best Student Paper Award at the 13th European Conference on Antennas and Propagation, Krakow, Poland, in 2019, the First Prize Student Paper Competition Award at the IEEE-MTTs International Conference on Numerical Electromagnetic and Multiphysics Modeling and Optimization for RF, Microwave, and Terahertz Applications, Seville, Spain, in 2017, and the AIA Price for the Best Engineering Master Thesis Award from the Royal Military Academy, Brussels, in 2015.

Christophe Craeye (Senior Member, IEEE) was born in Belgium, in 1971. He received the master's degree in electrical engineering and the B.Phil. degree from the Université Catholique de Louvain (UCLouvain), Ottignies-Louvain-la-Neuve, Belgium, in 1994, and the Ph.D. degree in applied sciences from UCLouvain, in 1998.

His Ph.D. was carried out in collaboration with the National Aeronautics and Space Administration (NASA) and the European Space Agency (ESA). From 1999 to 2001, he was a Post-Doctoral Researcher with the Eindhoven University of Technology, Eindhoven, The Netherlands. He was with the University of Massachusetts, Amherst, MA, USA, in 1999. He was with the Netherlands Institute for Research in Astronomy, Dwingeloo, The Netherlands, in 2001. In 2002, he started an antenna research activity with UCLouvain, where he is currently a Professor. He was with the Astrophysics and Detectors Group, University of Cambridge, Cambridge, U.K., in 2011. His research is funded by the Region Wallonne, the European Commission, ESA, the Fonds National de la Recherche Scientifique (FNRS), and UCLouvain. His current research interests include mutual coupling, finite antenna arrays, wideband antennas, small antennas, metasurfaces, and numerical methods for fields in periodic media, with applications to communication and sensing systems.

Dr. Craeye received the 2005–2008 Georges Vanderlinden Prize from the Belgian Royal Academy of Sciences in 2009. He was an Associate Editor of IEEE TRANSACTIONS ON ANTENNAS AND PROPAGATION, from 2004 to 2010 and IEEE ANTENNAS AND WIRELESS PROPAGATION LETTERS, from 2011 to 2017.